EFFECTS OF HEAT RELEASE ON TURBULENT JET FLOWS

Matthias Ihme and Heinz Pitsch
Department of Mechanical Engineering
Stanford University
Stanford, CA 94305, USA
mihme@stanford.edu

ABSTRACT

Large-eddy simulations of isothermal and reactive turbulent round jets at a jet Reynolds number of 14,720 have been performed to study the effects of heat release on jet dynamics and entrainment. Results for flow field statistics from the simulations are in good agreement with available experimental data. Effects of buoyancy and temperature-dependent molecular properties on the instantaneous flow field and statistical flow field quantities are investigated in separate numerical simulations. Mass flux and jet entrainment rates have been computed from the simulations. It is shown that the fluctuating mass flux, which is difficult to determine experimentally, amounts to as much as 15 % of the total mass flux.

INTRODUCTION

A classical example for free shear flows is the turbulent round jet issuing from a long pipe. This canonical flow has been extensively studied both experimentally (Lockwood & Moneib, 1980; Richards & Pitts, 1993; Dahm & Dimotakis, 1990; Muñiz & Mungal, 2001; Han & Mungal, 2001; Mi *et al.*, 2001) and analytically (Hinze, 1975; George, 1989; George & Davidson, 2004). The reasons for this interest are not only the geometrical simplicity, but also its technical relevance. Turbulent jets are used in many technical systems, such as burners and chemical reactors, in which mixing of different fluids is required. Mixing is controlled by the entrainment rate of the ambient fluid into the jet stream. The local entrainment rate can be defined as

$$C_\mathrm{e} = \frac{D^*}{\dot{m}_\mathrm{J}} \frac{\mathrm{d}\dot{m}}{\mathrm{d}x} \,, \tag{1}$$

with D^* denoting the equivalent source diameter:

$$D^* = \frac{2\dot{m}_\mathrm{J}}{\sqrt{\pi \rho_\infty J_\mathrm{J}}} \,, \tag{2}$$

where ρ is the density, J is the mean momentum flux, x is the stream-wise coordinate, and $\dot{m}$ is the mean mass flux. The subscripts "J" and "∞" denote quantities related to the jet nozzle and the co-flow, respectively.

The differences in the entrainment rates in reacting and non-reacting jets have been investigated experimentally by different groups (Ricou & Spalding, 1961; Hill, 1972; Becker & Yamazaki, 1978; Muñiz & Mungal, 2001; Han & Mungal, 2001). It is generally found that non-reacting jets approach a constant entrainment rate after a transition region, which is dependent on the nozzle exit conditions (Ricou & Spalding, 1961). The asymptotic value for C_e decreases with increasing co-flow velocity (Muñiz & Mungal, 2001).

Measurements in reacting jets with heat release, on the other hand, showed a reduction in the entrainment rate (Becker & Yamazaki, 1978; Muñiz & Mungal, 2001). An asymptotic value for C_e could not be determined from the measurements by Muñiz & Mungal (2001). In fact, they observed that the entrainment rate rises after about 40 jet diameters downstream. This observation is in agreement with work by Becker & Yamazaki (1978), where this effect has been attributed to buoyancy, which adds additional momentum to the jet.

Furthermore, it has been observed experimentally that the near field of a jet flame is considerably different compared with isothermal jets at similar exit conditions. The presence of a flame can result in significant laminarization in the near field of the jet, which has been attributed to the increase in the kinematic viscosity and the dilatation caused by heat release (Takagi *et al.*, 1980; Masri *et al.*, 1984). Yamashita *et al.* (1990, 1992) and Takeno (1994) performed a series of two-dimensional numerical simulations at low Reynolds numbers to study the effects of temperature-dependent molecular properties on the jet transition.

Despite the geometrical simplicity of such canonical jet flows, some important questions remain unanswered. Reason for this is that some flow field quantities, such as the jet entrainment rate or the velocity-density correlation, remain difficult to measure accurately. For instance, the simultaneous point-wise measurement of the velocity fluctuations and density perturbation remains experimentally challenging. It has been estimated by Muñiz & Mungal (2001) that this correlation can contribute to as much as 20 % to the local jet mass flux.

Other effect, such as buoyancy, particularly in flows with large density variations, are not entirely possible to eliminate. This can result in a transition of an initially momentum driven jet into a buoyancy driven one at finite downstream distance, and might lead to ambiguities in the data analysis.

Another experimental difficulty is the analysis of effects due to temperature-dependent variations of the molecular properties on the flow structures and integral flow quantities.

The objective of this work is to further the understanding of the behavior of turbulent reacting and non-reacting jets using numerical simulations. In particular, highly resolved large-eddy simulations (LES) are performed with the aim of addressing different questions.

Numerical simulations allows to separately analyze the influence of different physical effects on the flow field and its statistics. Therefore, a series of numerical simulations are performed, in which effects of buoyancy and the variation in molecular properties due to heat release are individually studied.

Considering this contribution as an opportunity to complement experimental measurements, we provide information about the correlation term in the mass flux integral, which is often neglected in experimental measurements. This data might be helpful in quantifying experimental uncertainties.

To justify this analysis, the LES methods and combus-

tion models applied in the simulations have been validated first. An experimental configuration is chosen which provides comprehensive experimental validation data for both isothermal and reactive jet flows. The exit Reynolds number, defined as $\mathrm{Re} = U_\mathrm{J} D_\mathrm{J}/\nu_\mathrm{J}$ is 14,720 and is kept constant for all simulations. The nozzle diameter is denoted by D_J and ν is the kinematic viscosity. The operating conditions for the isothermal jet are chosen so that comparisons with the experimental data of Mi *et al.* (2001) can be made. Similarly, the non-premixed reactive jet resembles the experimentally analyzed so-called DLR flame A. This nitrogen-diluted methane-hydrogen/air flame has been studied by Bergmann *et al.* (1998), Meier *et al.* (2000), and Schneider *et al.* (2003).

The remainder of the paper is organized as follows. After the presentation of the mathematical models, the experimental configuration and numerical setup is summarized. Thereafter, differences in the turbulent flow field structure between isothermal and reactive jets are analyzed and statistical results are presented. The paper finishes with conclusions.

MATHEMATICAL MODEL

A low-Mach number variable density LES formulation is employed, in which the Favre-filtered form of the continuity and momentum equations are solved:

$$\widetilde{\mathcal{D}}_t\overline{\rho} = -\overline{\rho}\nabla\cdot\widetilde{\boldsymbol{u}}\,, \tag{3a}$$

$$\overline{\rho}\widetilde{\mathcal{D}}_t\widetilde{\boldsymbol{u}} = -\nabla\overline{p} + \frac{1}{\mathrm{Re}}\nabla\cdot\overline{\underline{\underline{\sigma}}} - \nabla\cdot\overline{\underline{\underline{\sigma}}}^{\mathrm{res}} - \frac{1}{\mathrm{Fr}^2}\hat{\boldsymbol{e}}_x\overline{\rho}\,, \tag{3b}$$

where $\boldsymbol{u}$ is the velocity vector, p is the pressure, $\underline{\underline{\sigma}}$ is the viscous stress tensor, $\hat{\boldsymbol{e}}_x$ is the unit vector in stream-wise direction, and $\widetilde{\mathcal{D}}_t = \partial_t + \widetilde{\boldsymbol{u}}\cdot\nabla$ is the substantial derivative. The Froude number is denoted by $\mathrm{Fr} = U_\mathrm{J}/\sqrt{gD_\mathrm{J}}$, and the residual stress tensor $\overline{\underline{\underline{\sigma}}}^{\mathrm{res}} = \overline{\rho\widetilde{\boldsymbol{u}}\widetilde{\boldsymbol{u}}} - \overline{\rho}\widetilde{\boldsymbol{u}}\widetilde{\boldsymbol{u}}$ is modeled by a dynamic Smagorinsky model (Germano *et al.*, 1991; Lilly, 1992). Here, a Favre-filtered quantity $\widetilde{\psi}$ is defined as $\widetilde{\psi}(\boldsymbol{x}) = \overline{\rho}^{-1}\int\rho(\boldsymbol{x}')\psi(\boldsymbol{x}')G(\boldsymbol{x},\boldsymbol{x}';\Delta)\mathrm{d}\boldsymbol{x}'$, where G is the filter-kernel, and Δ is the filter-width. Favre-filtered quantities can be related to Reynolds-filtered variables, denoted by an overbar, by the relation $\overline{\rho}\widetilde{\psi} = \overline{\rho\psi}$. Note, that the equations have been non-dimensionalized with the jet nozzle diameter D_J and the bulk exit jet velocity U_J.

The combustion model for the prediction of the reactive flow field is briefly summarized here. More details of the model can be found in Pierce & Moin (2001, 2004) and Ihme *et al.* (2005, 2006). In the present LES, a flamelet/progress variable (FPV) model is employed (Pierce & Moin, 2004). In this model, all thermochemical quantities, denoted by $\boldsymbol{\psi}$, are a function of mixture fraction Z and reaction progress variable C, which is a linear combination of major product mass fractions. Then, the state relation can be written as

$$\boldsymbol{\psi} = \mathcal{G}_{\boldsymbol{\psi}}(Z, C)\,. \tag{4}$$

This state relation is obtained from the solution of the steady flamelet equations (Peters, 1983, 1984),

$$-\frac{\chi_Z}{2}\partial_Z^2\boldsymbol{\phi} = \dot{\boldsymbol{\omega}}\,, \tag{5}$$

where $\dot{\boldsymbol{\omega}}$ is the thermochemical source term of all species and temperature, denoted by the vector $\boldsymbol{\phi}$, and χ_Z is the scalar dissipation rate.

An expression for the Favre-filtered thermochemical quantities, required in Eq. (3), can be obtained by integrating Eq. (4) with a presumed joint probability density function (PDF) of mixture fraction, and progress variable. Here, the joint PDF is modeled by a beta-distribution for the mixture fraction, and the conditional PDF of the progress variable is modeled by a Dirac distribution. The joint PDF is then parameterized by $\widetilde{Z}, \widetilde{C}$, and the residual variance of the mixture fraction $\widetilde{Z''^2}$. Thus, the thermochemical state equation for application in LES can be written as

$$\widetilde{\boldsymbol{\psi}} = \widetilde{\mathcal{G}}_{\boldsymbol{\psi}}(\widetilde{Z}, \widetilde{Z''^2}, \widetilde{C})\,. \tag{6}$$

In addition to the solution of the Navier-Stokes equations, the FPV model requires the solution of the following transport equations for $\widetilde{Z}$ and $\widetilde{C}$:

$$\overline{\rho}\widetilde{\mathcal{D}}_t\widetilde{Z} = \frac{1}{\mathrm{Re}\,\mathrm{Sc}}\nabla\cdot(\overline{\rho}\widetilde{\alpha}\nabla\widetilde{Z}) - \nabla\cdot\overline{\boldsymbol{\sigma}}_Z^{\mathrm{res}}\,, \tag{7a}$$

$$\overline{\rho}\widetilde{\mathcal{D}}_t\widetilde{C} = \frac{1}{\mathrm{Re}\,\mathrm{Sc}}\nabla\cdot(\overline{\rho}\widetilde{\alpha}\nabla\widetilde{C}) - \nabla\cdot\overline{\boldsymbol{\sigma}}_C^{\mathrm{res}} + \overline{\rho}\widetilde{\dot{\omega}}_C\,, \tag{7b}$$

with $\mathrm{Sc} = \nu/\alpha$ denoting the Schmidt number, and Lewis-numbers of all species have been assumed to be unity. The residual scalar fluxes, $\overline{\boldsymbol{\sigma}}_Z^{\mathrm{res}}$ and $\overline{\boldsymbol{\sigma}}_C^{\mathrm{res}}$ are computed using a dynamic procedure (Pierce & Moin, 2004).

EXPERIMENTAL CONFIGURATION AND NUMERICAL SETUP

In this work, large-eddy simulations of isothermal and reacting turbulent jets are performed. The operation conditions for the isothermal jet are chosen so that comparisons with the experimental data by Mi *et al.* (2001) can be made. Data from their experiments, in which a jet emanates from a pipe will be used. The length of this pipe is sufficiently long to ensure that the flow is fully developed when the fluid exits the nozzle. The Reynolds number is 16,000. The passive scalar in their experiment is represented by heating the fluid which exits the nozzle.

A non-premixed jet flame configuration at similar operation conditions has experimentally been studied by Bergmann *et al.* (1998), Meier *et al.* (2000), and Schneider *et al.* (2003). The burner configuration of this N_2-diluted CH_4-H_2/air flame consists of a central fuel nozzle of diameter D_J surrounded by a co-flow nozzle of square shape. The jet fluid consists of a mixture of 22.1 % CH_4, 33.2 % H_2, and 44.7 % N_2 by volume with a stoichiometric mixture fraction of $Z_\mathrm{st} = 0.167$. The fuel bulk velocity is U_J =42.2 m/s. Co-flow air is supplied at an axial velocity of $7.11\times10^{-3}U_\mathrm{J}$. The Reynolds number is Re = 14,720.

The Favre-filtered conservation equations for mass, momentum, mixture fraction and progress variable are solved in a cylindrical coordinate system $\boldsymbol{x} = (x, r, \varphi)^\mathsf{T}$. The computational domain is $120D_\mathrm{J}\times40D_\mathrm{J}\times2\pi$ in axial, radial, and circumferential directions, respectively. The radial direction is discretized by 160 unevenly spaced grid points concentrated in the fuel nozzle. The grid in axial direction uses 320 points, and is, beginning at the nozzle exit, stretched downstream. The circumferential direction is equally spaced and uses 64 points. The total number of grid points used for the simulation is approximately 3.28 million.

The non-dimensional minimum and maximum filter widths in the domain are $\Delta_\mathrm{min} = 0.031$ (nozzle lip) and $\Delta_\mathrm{max} = 1.94$ (outermost grid cell at the outflow plane). The numerical resolution of the LES should be compared with the Taylor microscale λ_T and the Kolmogorov length-scale η. Under the assumption of isotropy, these scales can be estimated as $\lambda_\mathrm{T} = u'(\mathrm{Re}\,\varepsilon/15)^{-1/2}$ and $\eta = (\mathrm{Re}^3\,\varepsilon)^{-1/4}$ with $\varepsilon = \xi u'^3/\ell, \xi \approx 0.33, \ell \approx 0.226 r_{1/2}^u$ (Kothnur *et al.*,

Table 1: Reference parameters for the jet flow simulation. The parameter for the isothermal jet simulation are slightly different to that of Mi *et al.* (2001) in order to allow for comparison with reactive flow simulations.

Parameter, units	Isothermal jet	Reacting jet
U_J/U_∞	140	140
Re	14,720	14,720
λ_T	4.2×10^{-2}	1.2×10^{-1}
η	1.9×10^{-3}	9.3×10^{-3}

Table 2: Variation of parameters for the three different reactive flow simulations.

Case	Parameters
1	• Fr = 150.6 • temp.-dependent kinematic viscosity and diffusivity
2	• Fr = ∞ • temp.-dependent kinematic viscosity and diffusivity
3	• Fr = ∞ • const. kinematic viscosity and diffusivity, equal to that of fuel stream, Sc = 1

2002). The integral lengthscale is ℓ, u' is the rms velocity, ε is the dissipation rate, and $r^u_{1/2}$ is the jet half width. These characteristic lengthscales are evaluated at a location near the nozzle lip, with $r^u_{1/2} = 1/2$, $u' = 0.2$. At this location the kinematic viscosity increases due to heat release for the reactive jet, resulting in a local Reynolds number based on jet diameter and jet exit velocity of Re =1,800. The estimated lengthscales together with the parameters used in the simulation are summarized in Tab. 1. The lengthscale estimation indicates that the Taylor lengthscale is numerically well resolved and that $\Delta_\mathrm{min}/\eta \approx 3$ in the reactive jet flow simulation.

The turbulent inlet velocity profile is generated by separately performing a periodic pipe flow simulation, where a constant mass flow rate is enforced. Convective outflow conditions are used at the outlet and no-slip boundary conditions are employed at the lateral boundaries.

In this work, LES of isothermal and reactive jet flows are performed. In order to identify the effects due to buoyancy and temperature-dependent variations in the molecular properties onto the flow structure, three different reactive jet flow simulations are performed. In all of these reactive flow simulation, chemistry is described by the GRI 2.11 mechanism (Bowman *et al.*, 1997), consisting of 279 reactions among 49 species. While effects due to gravity are neglected for the cases 2 and 3, a finite Froude number of Fr = 150.6 is used in case 1. Effects of temperature-dependent kinematic viscosity and diffusivity are considered in case 1 and 2, and constant viscosity and diffusivity equal to that of the fuel stream with Sc = 1 are used in case 3. The differences between these three cases are summarized in Tab. 2.

In the following section, results from the LES are presented and compared to experimental data. Temporally and azimuthally averaged quantities are denoted by $\langle\widetilde{\psi}\rangle$ with

$$\langle\widetilde{\psi}\rangle(x,r) = \frac{1}{2\pi T}\int_t^{t+T}\int_0^{2\pi}\widetilde{\psi}(t,\boldsymbol{x})\mathrm{d}\varphi\mathrm{d}t\ , \tag{8}$$

and the resolved averaged variance $\langle\widetilde{\psi}'^2_<\rangle$ is computed from

$$\langle\widetilde{\psi}'^2_<\rangle(x,r) = \frac{1}{2\pi T}\int_t^{t+T}\int_0^{2\pi}\Big(\widetilde{\psi}(t,\boldsymbol{x}) - \langle\widetilde{\psi}\rangle(x,r)\Big)^2\,\mathrm{d}\varphi\mathrm{d}t\ , \tag{9}$$

where $\widetilde{\psi} = \langle\widetilde{\psi}\rangle + \widetilde{\psi}'_<$. The mean mass flux across a surface in jet-normal direction is defined as

$$\dot{m} = \underbrace{2\pi\int_0^{r^u_{95}}\langle\overline{\rho}\rangle\langle\widetilde{u}\rangle r\mathrm{d}r}_{\langle\dot{m}\rangle} + \underbrace{2\pi\int_0^{r^u_{95}}\langle\overline{\rho}'_<\widetilde{u}'_<\rangle r\mathrm{d}r}_{\dot{m}'_<}\ , \tag{10}$$

where u denotes the axial velocity component, and r^u_{95} is defined as

$$r^u_{95}(x) = \{r|\langle\widetilde{u}\rangle(x,r) = \langle u\rangle(x,0) - 0.95(\langle u\rangle(x,0) - U_\infty)\}\ . \tag{11}$$

RESULTS

Turbulent Near Field Structure. Representative instantaneous passive scalar near-field results for $x \leq 8$ are shown in Fig. 1 for (a) the isothermal jet experiment by Mi *et al.* (2001), (b) an isothermal jet simulation, and for reactive jet flow simulations with (c) temperature-dependent and (d) constant molecular properties. The near field of the isothermal flow emanating from a long pipe studied by Mi *et al.* (2001) is dominated by small-scale turbulent structures that have been attributed to the interaction of broad-band turbulent disturbances exiting from the fully developed pipe flow with narrow-band instabilities in the shear-layer. This interaction results in a suppression of large-scale vortex formation. A similar instantaneous scalar near field is obtained from the isothermal jet simulation (Fig. 1(b)). The core region breaks down at approximately the same stream-wise location as observed in the experiment.

Figure 1(c) shows the near field of the reactive jet simulation. The shear layer surrounding the jet core region is mainly dominated by quasi-laminar structures. The turbulence in this region is suppressed by the effect of heat release which results in dilatation and an increase in the molecular transport coefficients leading to a locally lower Reynolds number. To assess these effects individually, a reactive simulation has been performed where all molecular transport coefficients have been kept constant. The result is shown in Fig. 1(d). This figure shows that the shear layer surrounding the jet core region contains finer turbulent structures compared with Fig. 1(c). In fact, these shear layer structures are similar to these of the isothermal jet flow, suggesting that the laminarization, apparent in Fig. 1(c), is mainly caused by the increase in the molecular transport properties rather than dilatation effects. Volume expansion due to heat release solely results in a reduction in the axial velocity decay, manifested by the extended length of the core region.

Note, however, that the jet Reynolds number in the present configurations is about 15,000, and these conclusion might not be valid for jet flows at significantly higher Reynolds numbers.

Centerline Profiles. Figure 2 shows the evolution of the mean (top) and rms (bottom) axial velocity along the centerline for all jet flow simulations compared with experimental

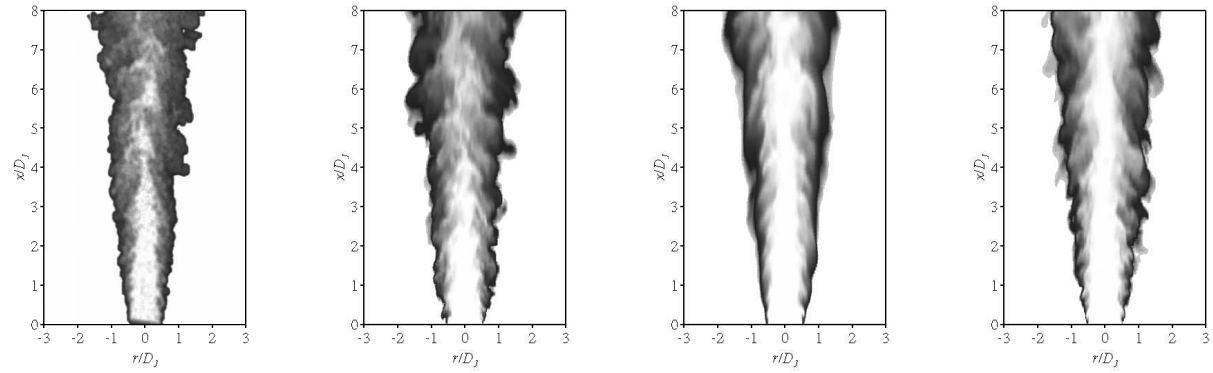

(a) isothermal jet experiment (b) isothermal jet LES (c) reactive jet LES (d) reactive jet LES with constant molecular properties

Figure 1: Comparison of instantaneous planar images of the passive scalar near-field obtained from (a) isothermal jet experiment (Mi *et al.*, 2001), (b) isothermal jet LES, non-premixed jet flame simulation with (c) temperature-dependent (case 2) and (d) constant molecular properties (case 3).

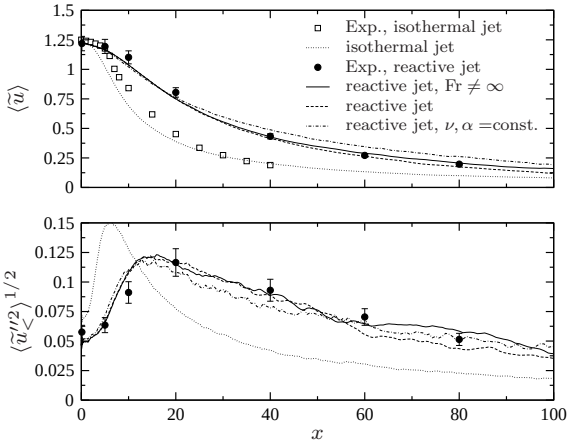

Figure 2: Comparison of the centerline mean and rms axial velocity decay predicted by the models with experimental data for isothermal and reacting jet.

results. Comparing first the isothermal jet simulation (dotted line) with experimental data (open symbols), it can be observed that the initial decay rate in the jet near field is over-predicted. The reason for this is the over-prediction of the initial shear layer width (not shown), which results in faster spreading and consequently to a reduction of the length of the core region.

Experimental results from the reactive jet flame are shown in solid symbols, and are compared with numerical simulations for cases 1 (solid line), 2 (dashed line), and 3 (dash-dotted line). Compared to the isothermal results, the mean and rms axial velocity decays slower for the reactive jet flow. This is a direct consequence of momentum conservation and density reduction due to heat release. From this follows that $u_{\mathrm{react}}/u_{\mathrm{isoth}} \propto (\rho_{\mathrm{isoth}}/\rho_{\mathrm{react}})^{1/2}$, where the subscripts "react" and "isoth" denote the reactive and isothermal conditions, respectively (Mungal, 2007). The effect of buoyancy (case 1, solid line) becomes apparent for $x \geq 40$; however, the small increase in the axial velocity due to buoyancy remains negligible for this momentum-driven jet. It is interesting to point out that the simulation with constant molecular transport properties (case 3) yields a considerably slower decay of the mean centerline velocity for $x \geq 20$. The lower kinematic viscosity and molecular diffusivity in that case results in a reduced jet spreading, and therefore to a higher centerline velocity by virtue of momentum conservation. Overall, the results obtained from the simulations which account for temperature-dependent molecular properties (cases 1 and 2) are in good agreement with velocity measurements by Schneider *et al.* (2003).

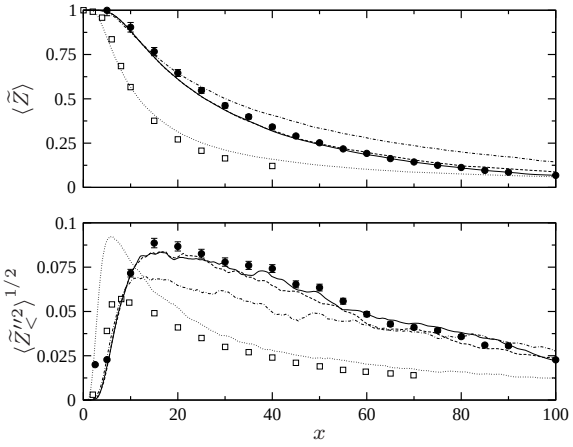

Figure 3: Comparison of the centerline mean and rms passive scalar decay between simulation and experimental data for isothermal and reacting jets. Refer to Fig. 2 for legend.

The evolution of the mean and rms passive scalar along the centerline are shown in Fig. 3. The mean passive scalar centerline evolution for the isothermal flow is in good agreement between experiment and simulation. The rms value is over-predicted in the jet near field.

The centerline profiles obtained from the reactive flow simulation are in good agreement with the experiment, indicated by the solid symbols. The buoyancy affects the passive scalar field by enhancing the scalar convection, and consequently leads to a reduction in the flame length. The flame length, defined as $L_{\mathrm{st}} = \{x|\langle\widetilde{Z}\rangle(x,0) = Z_{\mathrm{st}} = 0.167\}$, is extracted from the simulations and summarized in Tab. 3.

Note also that the simulation with constant molecular properties results in a slower decay of $\langle\widetilde{Z}\rangle$ and in a reduction in the peak rms value by approximately 20 %. The predicted rms passive scalar evolution for cases 1 and 2, shown in the lower panel of Fig. 3, are in good agreement with experi-

Table 3: Comparison between computed and experimentally determined flame length.

Case	Exp.	1	2	3
$L_{\rm st}$	64.3	63.6	67.5	90.8

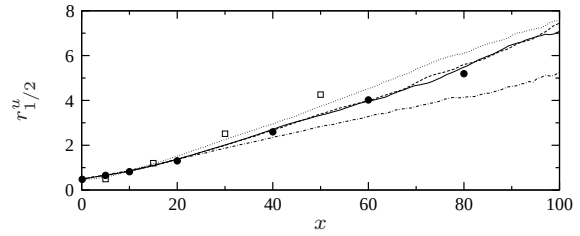

Figure 4: Stream-wise variation of the velocity half width for isothermal and reactive jets. Refer to Fig. 2 for legend.

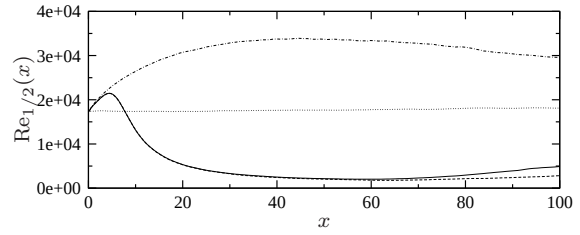

Figure 5: Stream-wise variation of the local Reynolds number, $\mathrm{Re}_{1/2}(x) = 2\langle\widetilde{u}\rangle(x,0)r^u_{1/2}(x)/\langle\widetilde{\nu}\rangle(0,r)$ for isothermal and reactive jets. Refer to Fig. 2 for legend.

mental data.

Jet Half Width and Local Reynolds Number. The stream-wise variation of the velocity half width is shown in Fig. 4. The spreading rate for the jet flame cases 1 and 2 are smaller than that of the isothermal jet. Compared to the experimental data, case 3 with constant molecular properties leads to a reduction of the jet half width by approximately 30 % in the far field region. Figure 5 shows that the slower velocity decay along the centerline and constant molecular properties for the reactive case 3 leads to higher local Reynolds number compared to the isothermal jet. On the other side, the strong dependence of the kinematic viscosity on the temperature for cases 1 and 2 results in a reduction of $\mathrm{Re}_{1/2}$ by approximately a factor of seven in the jet far field, compared to the isothermal jet.

Entrainment Rate. The computed mean mass flux and fluctuating mass flux for the isothermal and reactive jets are shown in Fig. 6.

The reactive jet flow cases 2 and 3 show a considerably lower mass flux compared to the isothermal jet. The reason for this is the competition between the slower velocity decay and the density reduction due to heat release. Following similar arguments as in the previous section, the mass flux ratio between isothermal and reactive jets can be estimated as $(\rho u)_{\rm react}/(\rho u)_{\rm isoth} \propto (\rho_{\rm react}/\rho_{\rm isoth})^{1/2}$.

Effects of buoyancy on the mass flux are also evident, resulting in increased mass flux. The axial mass flux for the case with constant molecular properties is significantly lower than that for case 2. This is attributed to the slower velocity decay and slower jet spreading rate, which is shown

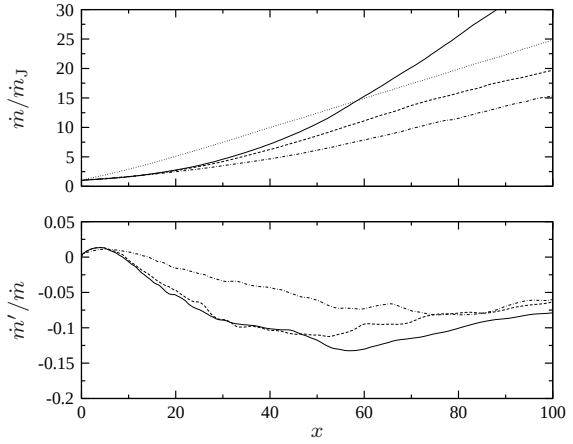

Figure 6: Normalized mean and fluctuating mass flux of the jet as function of the axial distance. Refer to Fig. 2 for legend.

in Figs. 2 and 4.

The calculated fluctuating mass flux as function of axial distance to the nozzle is shown in the bottom panel of Fig. 6. Muñiz & Mungal (2001) were not able to experimentally determine the term $\dot{m}'$ in Eq. (10) and estimated the resulting error as 20 %. The numerical simulation shows that $\dot{m}'/\dot{m}$ is typically less than 15 %, and has its maximum around the stoichiometric flame length. Note also that ρ' and u' are negatively correlated, which implies that the often experimentally determined term $\langle\dot{m}\rangle$ is larger than $\dot{m}$.

The computed jet entrainment rate $C_{\rm e}$ and experimental data from Han & Mungal (2001) (Re =18,000 and $U_{\rm J}/U_\infty = 109$) are shown in Fig. 7. Note that the axial coordinate is normalized with the equivalent source diameter. The non-reacting jet reaches a maximum entrainment

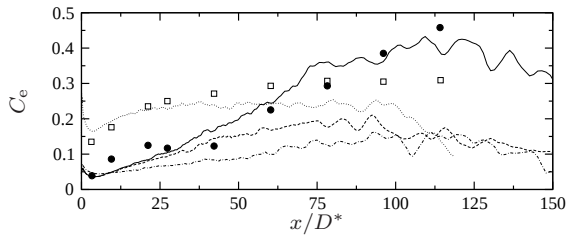

Figure 7: Entrainment rate of isothermal and reacting jets. Refer to Fig. 2 for legend.

rate of $C_{\rm e} = 0.24$ at about $30\,D^*$, and stays approximately constant until $x = 100\,D^*$. Compared with the isothermal jet, the entrainment rates for the reactive flow simulations without consideration of buoyancy grows until $x \approx 80D^*$, and slower decays thereafter. Buoyancy leads to an initially faster increase in the entrainment rate and reaches a maximum value of $C_{\rm e} = 0.41$ at approximately $x = 105\,D^*$.

CONCLUSIONS

In this paper, numerical simulations of reacting and non-reacting turbulent round jets are performed. In particular, effects due to gravity and due to the temperature-dependence of the molecular properties on the flow structure and statistical properties in the jet flame are analyzed. The results can be summarized as follows:

1. The simulation for both isothermal and reactive jets show good agreement with available experimental data for the centerline velocity and scalar decay, and also jet half widths.

2. The simulations showed that the quasi-laminarization of the shear layer surrounding the jet core region is mainly induced by the increase in viscosity and diffusivity due to heat-release, rather than dilatation effects.

3. Whereas centerline quantities and the jet spreading rate are relatively insensitive to gravity, a finite Froude number results in enhanced mass flux and therefore a higher jet entrainment rate, which is a consequence of the added momentum.

4. The contributions of the fluctuating mass flux to the overall mass flux have been computed for the different jet flames, indicating that this term amounts to as much as 15 % to the total mass flux. This is a particularly important information, since this term is usually neglected in experimental studies due its difficult measurement.

ACKNOWLEDGMENTS

The authors gratefully acknowledge funding by the United States Department of Energy within the Advanced Simulation and Computing (ASC) program. Helpful discussions with Prof. Godfrey Mungal are gratefully acknowledged.

REFERENCES

Becker, H. & Yamazaki, S. 1978 Entrainment, momentum flux and temperature in vertical free turbulent diffusion flames. *Combust. Flame* **33** (2), 123–149.

Bergmann, V., Meier, W., Wolff, D. & Stricker, W. 1998 Application of spontaneous Raman and Rayleigh scattering and 2D LIF for the characterization of a turbulent $CH_4/H_2/N_2$ jet diffusion flame. *Appl. Phys. B* **66** (4), 489–502.

Bowman, C., Hanson, R., Davidson, D., Gardiner, W., Lissianski, V., Smith, G., Golden, D., Frenklach, M. & Goldenberg, M. 1997 GRI-Mech 2.11. Available from `http://www.me.berkeley.edu/gri-mech/`.

Dahm, W. & Dimotakis, P. 1990 Mixing at large Schmidt number in the self-similar far field of turbulent jets. *J. Fluid Mech.* **217**, 299–330.

George, W. 1989 Self-preservation of turbulent flows and its relation to initial conditions and coherent structures. In *Advances in Turbulence* (ed. W. George & R. Arndt). Berlin: Springer-Verlag.

George, W. & Davidson, L. 2004 Role of initial conditions in establishing asymptotic flow behavior. *AIAA J.* **42** (3), 438–446.

Germano, M., Piomelli, U., Moin, P. & Cabot, W. 1991 A dynamic subgrid-scale eddy viscosity model. *Phys. Fluids A* **3** (7), 1760–1765.

Han, D. & Mungal, M. 2001 Direct measurement of entrainment in reacting/nonreacting turbulent jets. *Combust. Flame* **124** (3), 370–386.

Hill, B. 1972 Measurement of local entrainment rate in the initial region of axisymmetric turbulent air jets. *J. Fluid Mech.* **51** (4), 773–779.

Hinze, J. 1975 *Turbulence*, 2nd edn. McGraw-Hill.

Ihme, M., Bodony, D. & Pitsch, H. 2006 Prediction of combustion-generated noise in non-premixed turbulent jet flames using large-eddy simulation. *AIAA-2006-2614*.

Ihme, M., Cha, C. & Pitsch, H. 2005 Prediction of local extinction and re-ignition effects in non-premixed turbulent combustion using a flamelet/progress variable approach. *Proc. Combust. Inst.* **30**, 793–800.

Kothnur, P., Tsurikov, M., Clemens, N., Donbar, J. & Carter, C. 2002 Planar imaging of CH, OH, and velocity in turbulent non-premixed jet flames. *Proc. Combust. Inst.* **29**, 1921–1927.

Lilly, D. 1992 A proposed modification of the Germano subgrid-scale closure method. *Phys. Fluids A* **4** (3), 633–635.

Lockwood, F. & Moneib, H. 1980 Fluctuating temperature measurements in a heated round free jet. *Combust. Sci. Tech.* **22** (1-2), 63–81.

Masri, A., Starner, S. & Bilger, R. 1984 Transition and transport in the initial region of a turbulent diffusion flame. *Progress in Astronautics and Aeronautics* **95**, 293–304.

Meier, W., Barlow, R., Chen, Y. & Chen, J. 2000 Raman/Rayleigh/LIF measurements in a turbulent $CH_4/H_2/N_2$ jet diffusion flame: Experimental techniques and turbulence-chemistry interaction. *Combust. Flame* **123** (3), 326–343.

Mi, J., Nobes, D. & Nathan, G. 2001 Influence of jet exit conditions on the passive scalar field of an axisymmetric free jet. *J. Fluid Mech.* **432**, 91–125.

Muñiz, L. & Mungal, M. 2001 Effects of heat release and buoyancy on flow structure and entrainment in turbulent nonpremixed flames. *Combust. Flame* **126** (1-2), 1402–1420.

Mungal, M. 2007 Private communication.

Peters, N. 1983 Local quenching due to flame stretch and non-premixed turbulent combustion. *Combust. Sci. Tech.* **30**, 1–17.

Peters, N. 1984 Laminar diffusion flamelet models in non-premixed turbulent combustion. *Prog. Energy Combust. Sci.* **10** (3), 319–339.

Pierce, C. & Moin, P. 2001 Progress-variable approach for large eddy simulation of turbulent combustion. Report No. TF-80. Stanford University.

Pierce, C. & Moin, P. 2004 Progress-variable approach for large-eddy simulation of non-premixed turbulent combustion. *J. Fluid Mech.* **504**, 73–97.

Richards, C. & Pitts, W. 1993 Global density effects on the self-preservation behaviour of turbulent free jets. *J. Fluid Mech.* **254**, 417–435.

Ricou, F. & Spalding, D. 1961 Measurements of entrainment by axisymmetrical turbulent jets. *J. Fluid Mech.* **11** (1), 21–32.

Schneider, C., Dreizler, A., Janicka, J. & Hassel, E. 2003 Flow field measurements of stable and locally extinguishing hydrocarbon-fuelled jet flames. *Combust. Flame* **135** (1-2), 185–190.

Takagi, T., Shin, H. & Ishio, A. 1980 Local laminarization in turbulent diffusion flames. *Combust. Flame* **37** (2), 163–170.

Takeno, T. 1994 Transition and structure of jet diffusion flames. *Proc. Combust. Inst.* **25**, 1061–1073.

Yamashita, H., Kushida, G. & Takeno, T. 1990 A numerical study of the transition of jet diffusion flames. *Proc. R. Soc. London A* **431** (1882), 301–14.

Yamashita, H., Kushida, G. & Takeno, T. 1992 Characteristics of turbulent fluctuations in jet diffusion flames. *Proc. Combust. Inst.* **24**, 311–316.